Original research article

A self-adaptive learning method for motion blur kernel estimation of the single image

Wei Zhou [a,*], Xingxing Hao [a,*], Jin Cui [a], Yongxiang Yu [b], Xin Cao [a,*], Arjan Kuijper [c]

[a] *School of Information Science and Technology, Northwest University, Xi'an 710127, Shaanxi, China*
[b] *Department of Electrical and Automatic Engineering, East China Jiaotong University, Nanchang 330013, Jiangxi, China*
[c] *Fraunhofer IGD and TU Darmstadt, Darmstadt, Germany*

ARTICLE INFO

ABSTRACT

The estimation of blur kernel is the first and principal steps in the deconvolution of single blurred image. The quality of image restoration highly depends on its estimation accuracy. We then propose a new modified-Radon-transform approach along with a low-high-pass filtering method to estimate the motion blur parameters by a self-adaptive learning strategy, which greatly improved the deblurring quality of the blurred image. The Gaussian low-pass and high-pass filters are adopted to reduce the noise level in blurred image, and the batch normalization and self-adaptive method are considered to eliminate the interference from the noise stripes. It is noted that the estimation of blur angle plays an important cue for the exploration of blur kernel. The experimental evaluation is conducted on both synthetic VOC2012 database as well as the natural-real motion blurred single image with or without noise. The experimental results show that our proposed method can obtain more accurate and more reliable blur parameters than other approaches.

1. Introduction

Image blur caused by camera shake during exposure time is an inevitable problem in consumer photography, it has a great influence on various computer vision related areas, such as remote sensing, traffic monitor, medical imaging and public security [1–4]. In a general single image deblurring, a motion blurred image $b(x, y)$ with an additive noise $n(x, y)$ is usually modeled by the convolution between the latent image $\ell(x, y)$ and the point spread function (PSF) $k(x, y)$ [1]:

$$b(x, y) = \ell(x, y) * k(x, y) + n(x, y) \tag{1}$$

where $*$ is the convolution operator. If the blur kernel function $k(x, y)$ is known a priori, it is easily-feasible to recover the latent image $\ell(x, y)$ from the blurred one $b(x, y)$. However, in the problem of blurred image's deconvolution, both $k(x, y)$ and $\ell(x, y)$ are unknown, and both the unknowns needs to be estimated from a single $b(x, y)$. So, recovering $\ell(x, y)$ and $k(x, y)$ from the input $b(x, y)$ is a severely ill-posed problem, and the additive noise $n(x, y)$ makes it more challenging solving.

In recent years, there are mainly two kinds of the latest methods adopt neural network to deblur the degraded images [5–12]. The first types use the multi-frame images to construct a complex neural network, and mostly they are time-consuming [3,11–14]. Another ones are based on single images, and are compact in neural network structures [15–17], but they still own some weakness: Aizenberg et al. have developed a multi-layer neural network (MLMVN) to identify the blur kernel [6], but MLMVN almost focuses
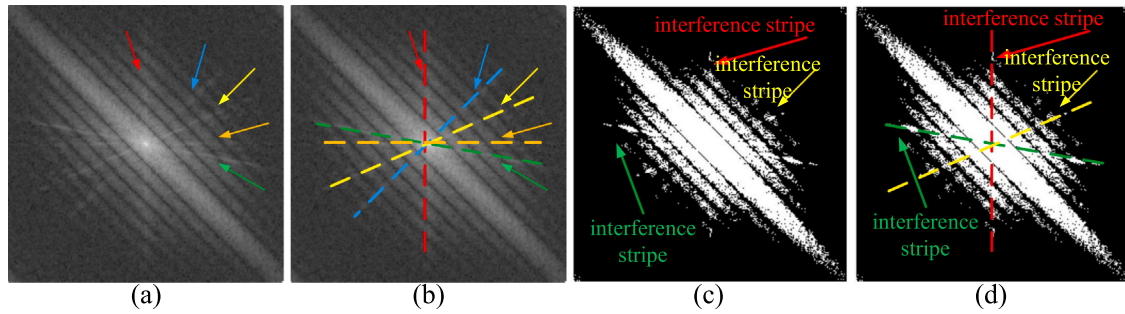
Fig. 1. (a)(b) The interference stripes in $B(u,v)$; (c)(d) The interference stripes in the binarization of the adaptive-filtered $B(u,v)$. (For interpretation of the references to color in this figure legend, the reader is referred to the web version of this article.)

on horizontal blur, and cannot solve the degraded images with the blur of other orientations [7]. Dash et al. developed radial basis function neural network (RBFNN) and Gabor filter to conduct the estimation of PSF's blur parameters [7], but they need to have enough Gabor filter masks in different directions to guarantee the accuracy of blur parameters [18]. Both of these two kinds of neural network methods are not applicable in the deblurring of single image. An appropriate way for deblurring the single image with motion blur is to conduct blind deconvolution with PSF on it.

The primary steps of blind image deconvolution is to estimate the PSF either separately or jointly with the restoration of degraded image [19,20], and the kernel issues for PSF are to detect the unknown motion parameters. Most of the PSF-based methods firstly adopt the spectrum response of blurred image to estimate the blur angle, and then rotate the blurred image inversely to detect the blur length [6,21–26]. So, the accurate estimation of the blur angle is of great significance for the deblurring of image. Amongst the existing techniques, many researches have been focused on estimating the blur parameters for deblurring. A method based on spectrum is proposed to estimate the blur parameters of linear-uniform and out-of-focus motion blurs with two modifications from the Radon transform, and this method performs well on the natural-real images [27]. A modified cepstrum based method adopts bit-plane slicing to estimate the blur parameters under uniform motion blur [28]. Cho et al. combines the Radon transform with the maximum a posteriori estimation to estimate the blur kernel, and the performance of this method is verified on a broader variety of circumstances [23]. To improve the robustness under noisy cases, a method based on Radon transform and bispectrum is proposed to estimate the blur parameters [29]. The Hough-transform-based methods for PSF estimation using the log spectrum of the blurred images are also presented in [30–32], these methods are flawed on the threshold selection of binarization, and the error estimation of blur angle will result in the error of blur length estimation [18]. Wang et al. combine bilateral-piecewise estimation and the sub-pixel level image to estimate the blur parameters under various noisy circumstances [18], but it is laborious for this method to explore effective solutions under non-linear and non-uniform motion blurs. Our recent work in [1] introduced a modification to the Radon transform for the estimation of blur kernel with the preprocessing of median filter, binarization and Soble edge detection, it also faces the challenges from the nonlinear and nonuniform motion blur problems. Most of the methods mentioned above still suffer low precision for blur parameters estimation under noisy cases especially when the spectrum image affected by the interference stripes (see also the color dotted line marking in Fig. 1).

Based on our recent work in [1], and inspired by the stripes in frequency response of single blurred image, a new modified-Radon-transform approach (Section 3) along with a low-high-pass filtering method (Section 2) is proposed to estimate the motion blur angle accurately from the single degraded image. Comparing with the recent work in blur kernel estimation [1], the following techniques adopted in this paper got more different and is more advanced.

- Firstly, we propose a low-pass filter with Gaussian function to filter the blurred image, which could reduce the noise level in image and weaken the impact from the interference stripes.
- Secondly, a new-defined high-pass filter is adopted to filter the frequency response of blurred image, thus could also weaken the influences from the noise and interference stripes.
- Thirdly, the batch normalization is implemented on the Radon transform of the frequency response to further eliminate the interference from the noisy stripes.
- Fourthly, the calculation of difference scores has been further optimized by a new equation (Eq. (10)).
- Fifthly, the finale selection process of blur angle is also optimized, and it is more robust and more reasonable.

2. The pipeline model of PSF and Radon transform

Assuming that the motion of the scene object is consistent with that of the camera, and the image is not affected by the additive noise, we can infer that the gray value of any point in the blurred image $b(x,y)$ is related to the gray value of the corresponding adjacent point in image $\ell(x,y)$. The general motion blurring kernel is expressed as in [18]:

$$k(x,y) = \begin{cases} \frac{1}{l}, & \text{if } \sqrt{x^2 + y^2} \leqslant \frac{l}{2} \text{ and } \frac{x}{y} = -\tan(\theta) \\ 0, & \text{otherwise} \end{cases} \tag{2}$$

The blur angle can be estimated by measuring the direction of the parallel dark stripes that appear in the frequency response of blurred images. Radon transform can detect lines in an image with no need to specify candidate points [29], which is defined as follows:

$$R\left(x', \theta\right) = \int_{-\infty}^{+\infty} b\left(x' \cos \theta - y' \sin \theta, x' \sin \theta - y' \cos \theta\right) dy' \tag{3}$$

where $R\left(x', \theta\right)$ indicates the projection value of Radon transform, θ is the angle of Radon transform. (x, y) and (x', y') represent the coordinates on image b and its Radon transformed image respectively. The relationship between (x, y) and (x', y') can be expressed as:

$$\begin{pmatrix} x' \\ y' \end{pmatrix} = \begin{pmatrix} \cos \theta & \sin \theta \\ -\sin \theta & \cos \theta \end{pmatrix} \begin{pmatrix} x \\ y \end{pmatrix} \tag{4}$$

As we mentioned previously, in the frequency response of motion blurred image, there are several parallel dark stripes slanting with a certain direction, which are also symmetrical. We can search the peak projection value of Radon transform for these parallel dark stripes in the frequency spectrum of blurred image, then the blur direction can be obtained. Most of the existing Radon transform methods do not preprocess the blurred image and its frequency response before adopting Radon transform to detect the blur direction, and they can handle most of the routines. However, the edge of the dark stripes in frequency response of blurred image are usually ambiguous when the degraded image are affected by the noise, and this will result in the error estimation of blur angle. This situation will affect the follow-up algorithm and even the quality of the whole image restoration. To avoid and solve this problem, we consider the application of low-pass and high-pass filters to our algorithms, and combine with a new Radon-transform-based method to detect the blur direction accurately.

3. The preprocessing of blurred image and its frequency

Before introducing our approach, we firstly analyze the negative impact from noise, camera and other image capturing facilities. Firstly, we try to transfer the blurred image b with Fourier transformation to obtain the frequency response $B(u, v)$, and we find that there are many interference stripes in $B(u, v)$ (see red, yellow, blue, green and dark-blue dash lines in Fig. 1(a)(b). To eliminate the interference from these irrelevant stripes, we attempt to filter and binarize $B(u, v)$ with adaptive median filter, and we can observe that the interference stripes are still remained in the binarization of the adaptive-filtered $B(u, v)$, but the number of the interference stripes is reduced to 3 in Fig. 1(c)(d). Although the above special measures has been applied to refine the results, the remained interference stripes still have the negative impacts on the estimation of blur direction.

We now show that our proposed low-pass and high-pass filters can be applied to a noise-blurred image, and improve the accuracy of blur direction estimation. Firstly, we consider the low-pass filter f_l to the blurred image $b(x, y)$:

$$b_l(\mathbf{p}) = b(\mathbf{p}) * f_l = \frac{1}{c} \int_{-\infty}^{\infty} w(t) b(\mathbf{p} + t) dt \tag{5}$$

where b and b_l represent a blurred image and its filtered image respectively, $\mathbf{p}$ is a pixel location, t is the distance from one pixel to $\mathbf{p}$, and c indicates the normalization factor which is defined as following:

$$c = \int_{-\infty}^{\infty} w(t) dt \tag{6}$$

$w(t)$ in Eqs. (5) and (6) is used to determine the profile of the filter, here we adopt a Gaussian function to achieve this function:

$$w(t) = exp(-t^2/2\sigma_f^2) \tag{7}$$

where σ_f is used to control the intensity of our low-pass filter. According to the Eq. (5), the smaller the value of σ_f, the greater the influence of noise, so increasing the value of σ_f can eliminate the influences of noise for blurred image, but too large value of σ_f will increase the blur level of the blurred image and introduce new interference. And in Eq. (8), the smaller the value of σ_f, the smaller the influence of adjacent interference stripes on the center stripe, and the greater the influence of faraway interference stripes on the center stripe. On balance, we set the value of σ_f to 0.5 Similar to the two-dimensional Gaussian filtering, f_l could average the pixels of blurred image b, and thus could reduce the noise level in image and affect the estimation of blur direction.

After we obtain the filtered blurred image $b_l(x, y)$ by our proposed low-pass filter, firstly we need to generate the frequency response $B_l(u, v)$ of $b_l(x, y)$ through Fourier transformation. Similar to what we did in the low-pass filter, we adopt the high-pass filter f_h to any point $\mathbf{q}$ in the frequency response $B_l(u, v)$ to obtain the filtered frequency spectrum B_h:

$$B_h(\mathbf{q}) = B_l(\mathbf{q}) * f_h = c \int_{-\infty}^{\infty} \frac{1}{w(t)} B_l(\mathbf{q} + t) dt \tag{8}$$

Following the steps in the previous analysis, we then adopt the adaptive median filter and adaptive-threshold binarization on B_h to obtain the binary spectrum B_{h2}. Then our self-adaptive Radon approach is conducted on the binary spectrum image B_{h2} to detect the direction of blur.
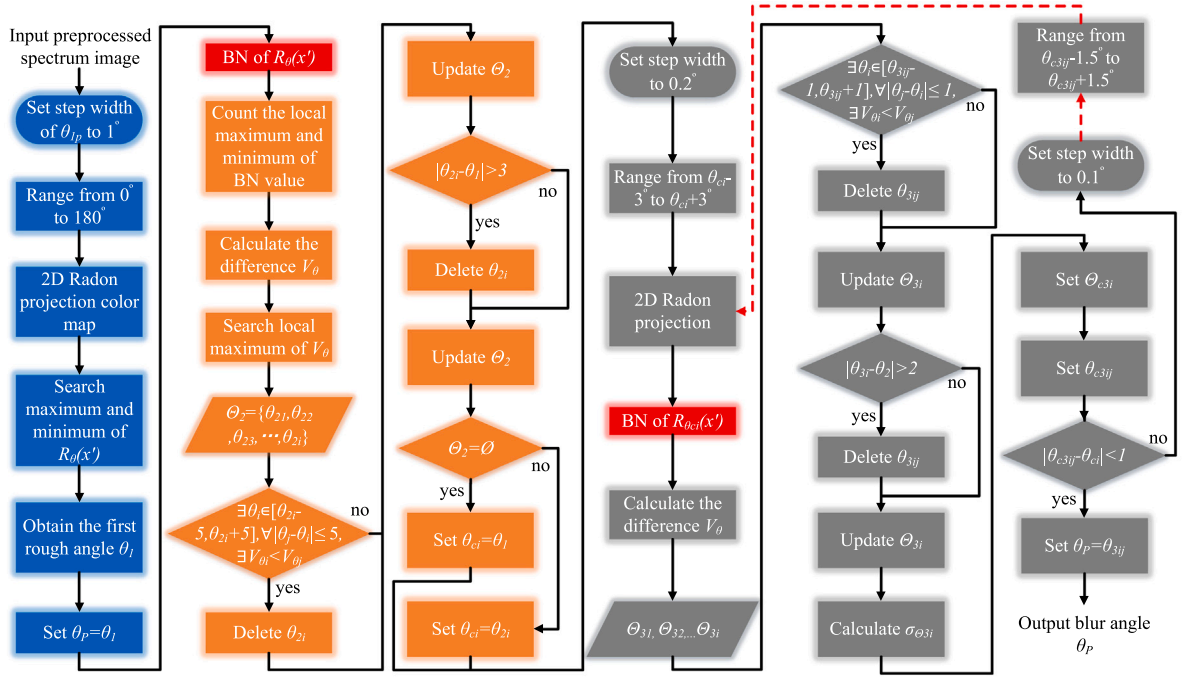
Fig. 2. Our self-adaptive Radon approach. (For interpretation of the references to color in this figure legend, the reader is referred to the web version of this article.)

4. Self-adaptive Radon approach

In this subsection we extend the Radon transformation to the application in the image deblurring and propose a self-adaptive Radon method to detect the blur direction. Before our self-adaptive Radon approach starts, the prepossessing of blurred image and its frequency is done, and we then obtain the preprocessed spectrum image B_{h2}. The outline of our self-adaptive Radon approach is presented in Fig. 2, the blue flow charts represent the first estimation of blur angle, the orange flow charts refer to the second estimation of blur angle, the gray flow charts are the third estimation of blur angle, and the red dotted lines are our self-adaptive accuracy improvement method.

During the first estimation of blur angle, we firstly set step width of θ_{1p} as 1° to generate 2D Radon projection color map by varying θ_{1p} from 0° to 180°. We can obtain the first rough angle θ_1 by searching the maximum and minimum of $R_\theta(x')$ in the 2D Radon projection color map of B_{h2}, since there are many maxima and minima for the Radon transform projection with blur angle in the color map. And we temporarily set the blur angle θ_P as θ_1 (see also in the blur flowcharts blocks in Fig. 2).

As the red flowcharts shown in Fig. 2, to eliminate the interference from the noisy stripes, we firstly apply batch normalization transform on $R_\theta(x') = \{R_{\theta_1}(x')...R_{\theta_m}(x')\}$ to obtain $\widehat{R}_\theta(x')$ as following:

$$\mu_R = \frac{1}{m}\sum_{i=1}^{m}R_{\theta_i}(x')$$

$$\sigma_R^2 = \frac{1}{m}\sum_{i=1}^{m}(R_{\theta_i}(x') - \mu_R)^2 \qquad (9)$$

$$\widehat{R}_{\theta_i}(x') = \frac{R_{\theta_i}(x') - \mu_R}{\sqrt{\sigma_R^2 + \epsilon_r}}$$

where μ_R, σ_R^2 are the mean value and variance of $R_\theta(x')$ respectively, m represent the amount of $R_\theta(x')$, and ϵ_r is a constant to avoid formula division by 0. Then we count the local maximum and minimum of $\widehat{R}_\theta(x')$. After the local maximum and minimum groups of $\widehat{R}_\theta(x')$ are obtained, we then calculate the difference score V_θ between the local maximum and minimum groups:

$$V_\theta = \frac{\mu_{max}^2 + \mu_{min}^2 + \epsilon_v}{2\mu_{max}\mu_{min} + \epsilon_v} \qquad (10)$$

where μ_{max}, μ_{min} are the mean value of the local maximum and minimum groups of $\widehat{R}_\theta(x')$ respectively, and ϵ_v is a constant to avoid the formula division by 0 in Eq. (10). Then we calculate all angles' V_θ by varying θ_{2p} from 0° to 180° with step width of 1°. We

Table 1
Estimation accuracy comparison between five methods for blur angle with or without our self-adaptive strategy.

Method	Moghaddam [29]		Tra-Radon [23]		RBFNN [7]		Wang [18]		Zhou [1]		Our method	
Preprocessed or not	No	Yes	No	Yes	No	Yes	No	Yes	No	Yes	No	Yes
Min.absolute error	0	0	0	/	0	/	0	0	0	0	**0**	**0**
Max.absolute error	2.013	1.924	0.986	/	0.885	/	0.262	0.231	0.222	0.209	**0.201**	**0.192**
Mean.absolute error	0.631	0.583	0.602	/	0.579	/	0.124	0.109	0.114	0.103	**0.110**	**0.099**

can obtain the angle set $\Theta_2 = \{\theta_{21}, \theta_{22}, \ldots, \theta_{2i}\}$ by searching the corresponding angle of the local maximum of V_θ:

$$\{\theta_{2i}|\forall\|\theta - \theta_{2i}\| \leq 10, \exists V_{\theta_{2i}} > V_\theta\} \Rightarrow \theta_{2i} \in \Theta_2 \tag{11}$$

Θ_2 will contain the false positive (FP) elements, since the spectrum images contain the interference stripes. To reduce the influence of clutter stripes, we delete the FP elements in Θ_2 with following constraints:

$$\text{update } \Theta_2 \begin{cases} (1)\exists\theta_i \in [\theta_{2i} - 5, \theta_{2i} + 5], \forall\|\theta_j - \theta_i\| \leq 5, \exists V_{\theta_i} < V_{\theta_j}, & \textbf{delete} \quad \theta_{2i} \\ (2)\|\theta_{2i} - \theta_1\| > 3, & \textbf{delete} \quad \theta_{2i} \\ (3)otherwise, & \textbf{remain} \quad \theta_{2i} \end{cases} \tag{12}$$

In Eq. (12), the larger these constrain integer values are, the easier it is to remain the FP. On the other hand, the smaller these constrain integer values are, the easier it is to remove the TP. On balance, we choose 5 and 3 for these constrain values respectively. Then we set every element in Θ_2 as the candidates θ_{ci} of blur angle. Besides, in order to avoid the process disruption of blur angle estimation, we temporarily set θ_1 as the candidate θ_{ci} of blur angle if Θ_2 is an empty set.

As the gray flowcharts shown in Fig. 2, based on the candidates θ_{ci} of blur angle from Θ_2 or θ_1, we firstly obtain the Radon transformations $R_{\theta_{ci}}(x')$ for the spectrum image with the angles from $\theta_{ci} - 3°$ to $\theta_{ci} + 3°$, and the step width is set to $0.2°$. Similar to the initial operation in the orange flowcharts, we also conduct the batch normalization transform on $R_{\theta_{ci}}(x') = \{R_{\theta_1}(x')...R_{\theta_n}(x')\}$ to obtain $\hat{R}_{\theta_{ci}}(x')$ by Eq. (9), and use Eq. (10) to calculate all angles' difference score V_θ. Through searching the corresponding angle of the local maximum of V_θ, we can obtain the angle set $\Theta_{3i} = \{\theta_{3i1}, \theta_{3i2}, \ldots, \theta_{3ij}\}$:

$$\{\theta_{3ij}|\forall\|\theta - \theta_{3ij}\| \leq 10, \exists V_{\theta_{3ij}} > V_\theta\} \Rightarrow \theta_{3ij} \in \Theta_{3i} \tag{13}$$

To eliminate the FP results in Θ_{3i}, we set the following constraints:

$$\text{update } \Theta_{3i} \begin{cases} (1)\exists\theta_i \in [\theta_{3ij} - 1, \theta_{3ij} + 1], \forall\theta_j \in [\theta_i - 1, \theta_i + 1], \exists V_{\theta_i} < V_{\theta_j}, & \textbf{delete} \quad \theta_{3ij} \\ (2)\|\theta_{3ij} - \theta_{ci}\| > 2, & \textbf{delete} \quad \theta_{3ij} \\ (3)otherwise, & \textbf{remain} \quad \theta_{3ij} \end{cases} \tag{14}$$

Following the criteria in Eq. (12), we set the constrain values in Eq. (14) to 1 and 2 respectively. After we have updated $\Theta_{31}, \Theta_{32}...\Theta_{3i}$ for each candidate θ_{ci}, the empty sets among $\Theta_{31}, \Theta_{32}...\Theta_{3i}$ will be abandoned. For all the remaining angle set $\Theta_{31}, \Theta_{32}...\Theta_{3i}$, we choose the set with the least variance $\sigma_{\Theta_{3i}}$ as the candidate angle set $\Theta_{c3i} = \{\theta_{c3i1}, \theta_{c3i2}....\theta_{c3ij}\}$:

$$\sigma_{\Theta_{3i}} = \sqrt{\frac{1}{n}\Sigma_{j=1}^n(\theta_{3ij} - \theta_{ci})^2} \tag{15}$$

For all elements in the angle set Θ_{c3i}, we choose the angle θ_{c3ij} with the smallest difference between θ_{c3ij} and its corresponding interval center θ_{ci} as the most suitable candidate angle.

In addition, we conduct a self-adaptive accuracy improvement method to increase the precision of the estimated blur angle, as the red dotted lines shown in Fig. 2. We set a constraint to determine whether the self-adaptive accuracy improvement method is necessary to be run. If the absolute value of the difference between θ_{c3ij} and its corresponding interval center θ_{ci} is greater than 1 ($\|\theta_{c3ij} - \theta_{ci}\| \geq 1$), the self-adaptive accuracy improvement method will be implemented, otherwise skip this method and set the blur angle $\theta_P = \theta_{c3ij}$. When $\|\theta_{c3ij} - \theta_{ci}\| \geq 1$, the algorithm will loop from the beginning of the gray flowchart with the angles from $\theta_{c3ij} - 1.5°$ to $\theta_{c3ij} + 1.5°$, and the step width is set to $0.1°$. Only when θ_{c3ij} satisfies the constraint condition can the algorithm output the blur angle.

5. Experiments and discussions

A set of comparisons between our proposed algorithm and the state-of-the-art approaches (Moghaddam [29], traditional Radon-transform-based method [23], artificial neural network approach (ANN) RBFNN [7], Wang [18], Zhou [1](our previous work)) are implemented on a total of 18625 images consisting of VOC2012 dataset [33] and real-life pictures.
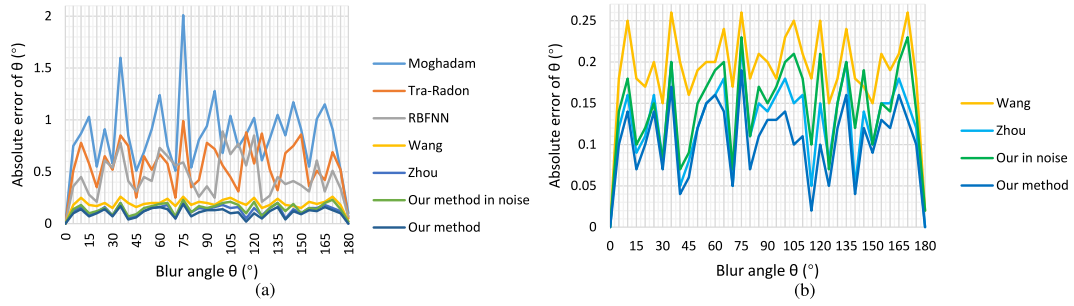
Fig. 3. (a) Absolute error comparison of blur angle between Moghaddam [29], traditional Radon-transform-based method [23], RBFNN [7], Wang [18], Zhou [1] and our proposed new method. (b) The local enlarged version of (a).
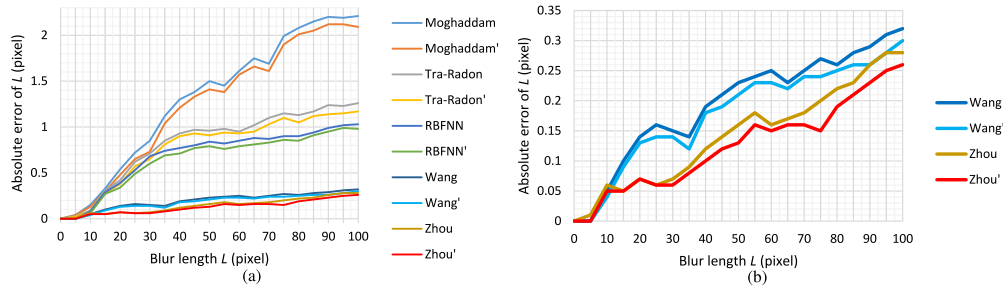

Fig. 4. (a) The effect of our self-adaptive strategy on Moghaddam [29], traditional Radon-transform-based method [23], RBFNN [7], Wang [18] and Zhou [1] (the legend One' is the experimental results of our self-adaptive learning strategy combined with the blur length estimation of it, e.g. Moghaddam'). (b) The local enlarged version of (a).

5.1. Blur angle estimation

In this part, our proposed blur angle estimation methods are evaluated through the degraded images which are created by varying the blur angle from 0° to 180° and the blur length from 0 to 100 pixels respectively.

Firstly, we conduct the blur angle experiments for each method. In this experiment, to be fair and in order to highlight our self-adaptive learning strategy, the frequency-based methods Moghaddam, Wang and Zhou's algorithms are also integrated with our proposed self-adaptive learning strategy, traditional Radon-transform-based method and RBFNN are implemented without our self-adaptive learning strategy, since they are not based on frequency response of image. Moreover, the Gaussian noise with standard deviation of 0.0001 is also added into the blurred images to evaluate and validate the superiority of our proposed method. The absolute error comparison of blur angle estimation between the five methods are presented in Table 1 and Fig. 3. In order to see the difference between the several methods more clearly, we enlarge Fig. 3(a) and place it in Fig. 3(b). From the results, we can obtain several observations:

1. In this experiment, all methods can achieve zero error for minimum absolute errors of blur angle.
2. In sharp contrast, after using our self-adaptive learning strategy, the absolute errors of Moghaddam, Wang, Zhou and our method are all reduced, especially Moghaddam.
3. No matter in which situations, our approach achieves the best results for blur angle estimation with the least mean absolute errors of 0.099 under the assistance of the self-adaptive learning strategy. In addition, the maximum absolute errors of blur angle produced by our approach are less than 0.192, and this is significantly smaller than those generated by the other comparison methods.

Moreover, we replace the blur angle estimation algorithms in Moghaddam [29], traditional Radon-transform-based method [23], RBFNN [7], Wang [18], Zhou [1] with our self-adaptive learning strategy proposed in this paper to further verify the superiority of our proposed strategy. This experiment is conducted by varying blur length from 0 to 100 pixels with a step of 5 pixels at a random blur angle respectively. Firstly, we adopt our self-adaptive learning methods and the ones in the other four methods to estimate the blur angle of the degraded image. Then we combine our self-adaptive learning methods with these four methods' blur length estimation algorithms to prove the effect of our self-adaptive learning strategy. Under this circumstance, the absolute errors with respect to the blur length are observed, the experimental results for the evaluation of our self-adaptive learning methods are presented in Fig. 4. In Fig. 4, the legend One (e.g. Moghaddam) is the results of Moghaddam [29], traditional Radon-transform-based method [23], RBFNN [7] and Wang [18] without using our self-adaptive learning methods, and the legend One'(e.g. Moghaddam') is the experimental results of our self-adaptive learning strategy combined with the blur length estimation of Moghaddam [29],
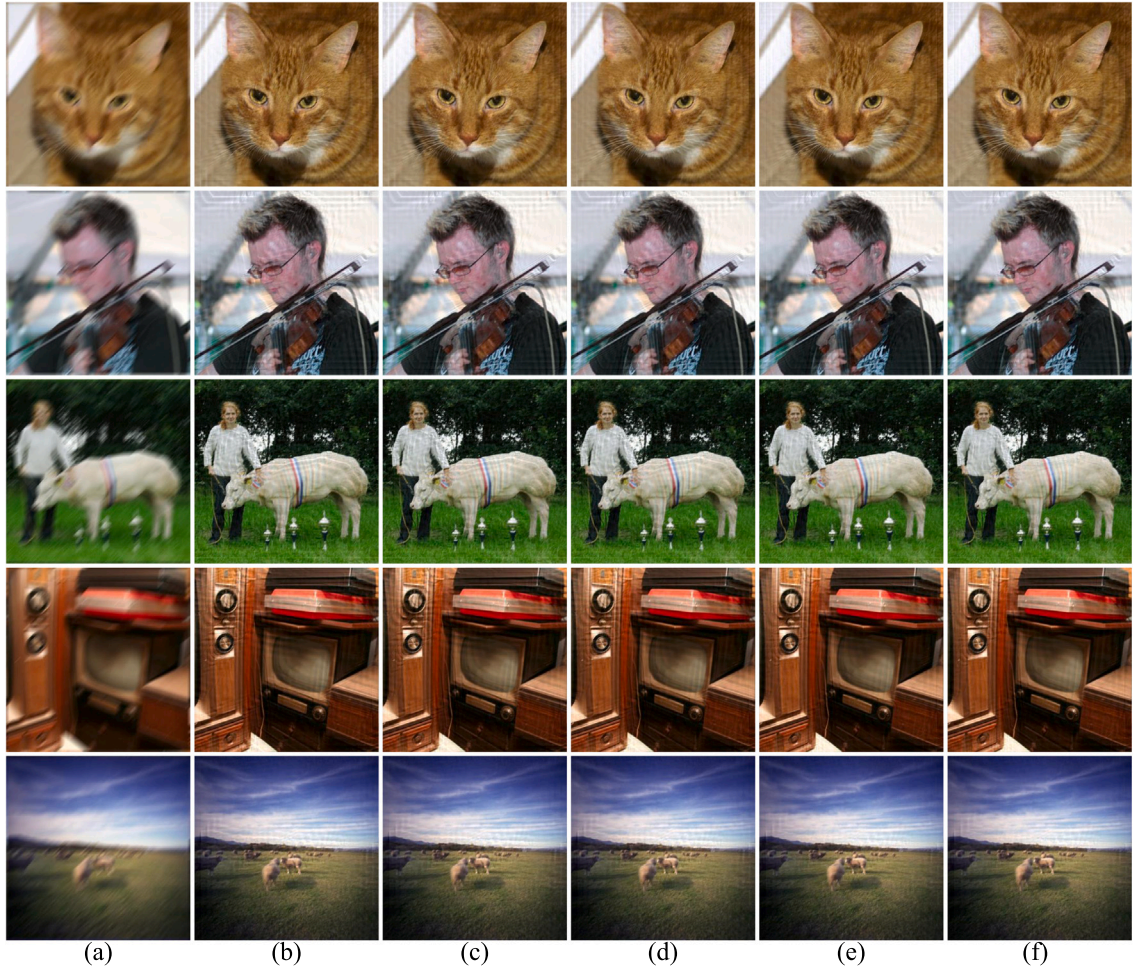
Fig. 5. Samples of deblurring results with different methods on noise-free VOC2012 dataset. (a) degraded image, (b) traditional Radon-transform-based method's result, (c) RBFNN's results, (d) Wang's results, (e) Zhou's results, (f) our results.

traditional Radon-transform-based method [23], RBFNN [7] and Wang [18], e.g. Moghaddam', Tra-Radon', RBFNN' and Wang'. Similar to Fig. 3, to see the difference between each method more clearly, we also enlarge Fig. 4(a) and place it in Fig. 4(b). From the results, we can see that the improvements performances of all methods with our self-adaptive learning methods are not obvious when the blur lengths are below 30. But when the blur lengths varies in the range of 30–100, compared with their own approaches, it is obvious that all methods' absolute error decreases significantly after adopting our self-adaptive learning strategy. All these observations confirm the high performances of our proposed methods.

5.2. Deblurring of noise-free images

In this section, we combine our own method with the blur length detection approach of Wang [18] to construct the PSF function, and then use the regularized filter to restore the deblurred image, thus validate that our algorithm could yield more superior performances of deblurring than the state-of-the-art methods. In order to reach this purpose, we will compare our method against traditional Radon-transform-based method [23], RBFNN [7], Wang [18] and Zhou [1] on VOC2012 dataset [33] and real-life degraded images.

In the VOC2012 dataset experiment, we employ peak signal-to-noise ratio (PSNR), structural similarity index (SSIM) and the time efficiency as the quantitative evaluation criteria for all methods' demonstration. PSNR is defined as:

$$\text{MSE} = \frac{1}{MN} \sum_{x=1}^{M} \sum_{y=1}^{N} (f(x, y) - \hat{f}(x, y))^2 \tag{16}$$

$$\text{PSNR} = 10 \log_{10} \left(\frac{255^2}{\text{MSE}} \right) \tag{17}$$

Table 2

PSNR (dB), SSIM and the running time (in seconds) of each method on noise-free VOC2012 database.

Method	Tra-Radon [23]			RBFNN [7]			Wang [18]			Zhou [1]			Our method		
Image	PSNR (dB)	SSIM (%)	Time (s)	PSNR (dB)	SSIM (%)	Time (s)	PSNR (dB)	SSIM (%)	Time (s)	PSNR (dB)	SSIM (%)	Time (s)	PSNR (dB)	SSIM (%)	Time (s)
2007_002852	74.71	82.25	62.34	74.84	82.52	56.48	75.61	83.86	11.45	75.61	83.85	10.71	**76.81**	**85.88**	**10.20**
2007_003194	73.77	89.14	65.48	73.89	89.36	59.88	74.69	90.61	11.97	74.67	90.60	10.44	**75.84**	**91.89**	**9.78**
2007_006232	69.43	70.31	61.82	69.57	70.88	61.37	70.46	74.35	12.25	70.47	74.36	10.87	**71.54**	**76.28**	**10.42**
2008_000748	75.62	92.58	59.94	75.80	92.78	58.45	76.99	93.96	12.08	77.00	93.96	10.31	**78.31**	**96.76**	**9.52**
2008_000868	69.42	73.41	57.38	69.54	73.86	61.05	70.24	76.30	12.45	70.25	76.30	10.56	**71.45**	**78.41**	**10.38**
2008_001389	71.75	91.88	62.79	71.88	92.05	58.69	72.74	93.01	14.02	72.74	93.00	12.11	**73.98**	**94.52**	**11.08**
2008_001625	70.25	73.63	62.35	70.40	74.17	59.75	71.29	77.30	12.35	71.30	77.30	10.91	**73.51**	**79.98**	**10.45**
2009_000634	70.50	68.64	59.54	70.65	69.28	57.02	71.60	73.14	12.23	71.60	73.16	11.21	**72.85**	**75.31**	**11.05**
2009_000692	77.16	97.39	60.84	77.36	97.47	60.28	78.60	97.85	11.87	78.61	97.87	11.52	**79.82**	**98.54**	**10.92**
2009_001443	70.52	73.36	59.49	70.65	73.86	58.36	71.46	76.88	12.55	71.46	76.89	11.04	**74.61**	**78.67**	**9.99**
2009_001517	74.06	81.99	56.57	74.21	82.38	58.65	75.17	84.95	12.37	75.18	84.98	10.83	**76.27**	**87.48**	**10.52**
2010_000069	73.37	86.32	54.32	73.55	86.68	61.36	74.85	89.06	12.59	74.87	89.10	10.64	**75.95**	**90.56**	**10.75**
2010_000805	78.43	96.47	53.58	78.61	96.57	59.85	79.85	97.10	12.52	79.85	97.09	10.76	**80.31**	**99.21**	**10.82**
2010_005277	70.42	82.07	54.35	70.53	82.44	61.89	71.19	84.47	12.90	71.18	84.46	10.99	**73.08**	**86.32**	**9.97**
2010_006181	73.60	76.90	53.89	73.73	77.33	57.25	74.55	79.83	13.35	74.54	79.82	11.44	**76.78**	**81.27**	**11.24**
2011_002341	74.31	90.12	56.73	74.42	90.35	56.69	75.05	91.61	12.51	75.05	91.60	10.92	**77.56**	**94.56**	**10.50**
2011_003177	73.60	77.65	53.79	73.73	78.03	59.42	74.54	80.48	11.30	74.53	80.46	10.31	**76.62**	**82.31**	**10.24**
2012_000778	71.20	77.08	55.91	71.32	77.56	57.36	72.07	80.31	12.49	72.06	80.24	10.61	**74.89**	**84.52**	**9.98**
Overall	72.90	82.29	58.40	73.04	82.64	59.10	73.94	84.73	12.40	73.94	84.72	10.90	**75.57**	**86.80**	**10.43**

where $f(x, y)$ and $\hat{f}(x, y)$ are the original clear image and the recovered image respectively, MSE is the mean square error, M and N are the size of image. SSIM is calculated as:

$$\text{SSIM}(f, \hat{f}) = \frac{\left(2\mu_f \mu_{\hat{f}} + C_1\right)\left(2\sigma_{f\hat{f}} + C_2\right)}{\left(\mu_f^2 + \mu_{\hat{f}}^2 + C_1\right)\left(\sigma_f^2 + \sigma_{\hat{f}}^2 + C_2\right)} \qquad (18)$$

where μ_f and $\mu_{\hat{f}}$ are the means of images f and $\hat{f}$ respectively, σ_f, $\sigma_{\hat{f}}$ and $\sigma_{f\hat{f}}$ stand for the standard deviations and cross-covariance for images f and $\hat{f}$, and C_1 and C_2 are two constants to avoid division of formula by 0. Normally, the larger PSNR and SSIM, the higher deblurring quality. That means, an ideal result of PSNR is infinity, and an optimal SSIM owns the value of 1.

The PSNR, SSIM and the calculated time of each method over the sample pictures of VOC2012 are shown in Table 2. It is clear that our algorithms has a great advantage in acquiring better results of PSNR and SSIM on all sample images than Wang's approach and our previous work (Zhou), the performance of traditional Radon-transform-based algorithm and RBNFF followed Wang in turn. In time efficiency, although additional-optimized operations have been added in our proposed methods in this paper (e.g., Gaussian low-pass and high-pass filters), our methods still achieve the fastest speed on the sampled pictures. Compared with our proposed methods, our previous work and Wang's methods, traditional Radon-transform-based algorithm and RBNFF are extremely time-consuming. Furthermore, in order to demonstrate the experimental results more intuitively, the blurred images and deblurring results generated by these five methods in noise-free VOC2012 database are illustrated in Fig. 5. From the results, we can also observe that our proposed algorithms gained satisfactory deblurring results over different images, and traditional Radon-transform-based algorithm and RBNFF fail to fully eliminate the blurring effects in the degraded pictures, this is roughly consistent with the performances in Table 2.

In order to further verify the superiority of our proposed method, the experiments of deblurring for all algorithms on the real-captured-degraded images are implemented. These degraded pictures are acquired by hand-held camera with random shaking. Among them, the car image is captured in a moving car on the road, and the picture of Eiffel Tower is obtained from a moving cruise ship. In this experiment, the blind deconvolution is utilized to deblur the blurred image with the detected PSF function. The experimental results are shown in Fig. 6. Through the visualized results in Fig. 6, we can find the similar advantage of our proposed method presented in the previous experiments in this section.

5.3. Deblurring of noise images

After the noise-free experiments, we implement a series of tests on noise-blurred images to further prove the superior performance of our proposed algorithms by measuring the PSNR and SSIM of the noise-blurred images' restoration results. The pictures of VOC2012 are firstly blurred by the filtering of random PSF function, and then the Gaussian noise of standard deviation $\sigma = 0.0001$ is attached to generate the noise-blurred images. In fairness, all methods in this experiment adopt blind deconvolution to filter the degraded pictures with their own estimated PSF. Parts of the experimental results with the deblurred images and the evaluation indexes are presented in Fig. 7 and Table 3. According to the visualized experimental results, we can observe that the images recovered by Wang, Zhou and our algorithm demonstrate more superior performances than other methods. Moreover, through the image evaluation indexes (PSNR and SSIM) of the deblurred images recovered by each method in Table 3, we can observe that our algorithm yields the highest evaluation indexes on VOC2012 with Gaussian noise except 2010_000069.jpg, and we reach the highest indexes values in the database as a whole. These results show that our method is better than the other four methods in noise cases.

Fig. 6. Restoration with different methods on the real natural blurred images. (a) degraded image, (b) Traditional Radon-transform-based method's results, (c) RBFNN's results, (d) Wang's results, (e) Zhou's results, (f) our results.

Table 3
PSNR (dB) and SSIM of each method on noise VOC2012 database.

Method	Tra-Radon [23]		RBFNN [7]		Wang [18]		Zhou [1]		Our method	
Image	PSNR (dB)	SSIM (%)	PSNR (dB)	SSIM (%)	PSNR (dB)	SSIM (%)	PSNR (dB)	SSIM (%)	PSNR (dB)	SSIM (%)
2007_002852	69.28	55.01	69.46	55.76	70.17	58.72	70.21	59.55	**70.46**	**60.06**
2007_003194	69.18	68.20	69.37	69.02	70.09	71.90	70.17	72.45	**70.36**	**73.13**
2007_006232	66.80	50.21	67.09	51.51	68.15	55.84	68.25	56.41	**68.34**	**56.87**
2008_000748	69.44	61.99	69.61	62.55	70.34	65.07	70.31	64.90	**70.64**	**66.40**
2008_000868	67.00	54.73	67.23	55.69	68.12	59.36	68.10	59.02	**68.31**	**60.37**
2008_001389	68.41	75.93	68.62	76.46	69.51	78.71	69.49	78.19	**69.75**	**79.67**
2008_001625	67.45	53.94	67.73	55.22	68.73	59.45	68.81	59.91	**68.94**	**60.50**
2009_000634	67.52	47.88	67.81	49.28	68.86	53.85	68.81	53.58	**69.08**	**54.96**
2009_000692	69.32	83.58	69.49	84.03	64.95	84.54	68.76	88.29	**72.79**	**91.76**
2009_001443	67.63	47.24	67.90	48.26	68.88	52.10	68.74	51.88	**69.08**	**53.29**
2009_001517	69.26	47.49	69.47	48.28	70.30	51.48	70.44	51.90	**70.59**	**52.95**
2010_000069	68.81	61.51	69.06	62.38	69.98	71.59	65.55	62.16	**71.05**	**73.47**
2010_000805	70.03	79.13	70.16	79.50	70.76	81.08	70.94	81.59	**71.06**	**81.93**
2010_005277	67.68	63.51	67.90	64.54	68.73	68.15	68.83	68.74	**68.91**	**69.17**
2010_006181	69.22	42.88	69.42	43.78	70.19	46.95	70.25	47.75	**70.46**	**48.30**
2011_002341	69.63	71.36	69.78	71.99	70.42	74.72	70.59	75.10	**70.68**	**75.82**
2011_003177	69.05	43.52	69.26	44.46	70.05	48.11	70.24	49.05	**70.31**	**49.53**
2012_000778	67.90	50.77	68.13	51.77	68.95	55.44	68.99	56.01	**69.15**	**56.60**
Overall	68.53	58.82	68.74	59.69	69.28	63.17	69.30	63.14	**70.05**	**64.71**

6. Conclusions

We considered a blur kernel estimation method for blind deconvolution of single image which is affected by motion blur, additive noise and interfered stripes. To address this problem and based on our previous work [1], a new modified-Radon-transform approach along within a Gaussian low-high-pass filtering method is proposed, which is inspired by the parallel and symmetric stripes in the
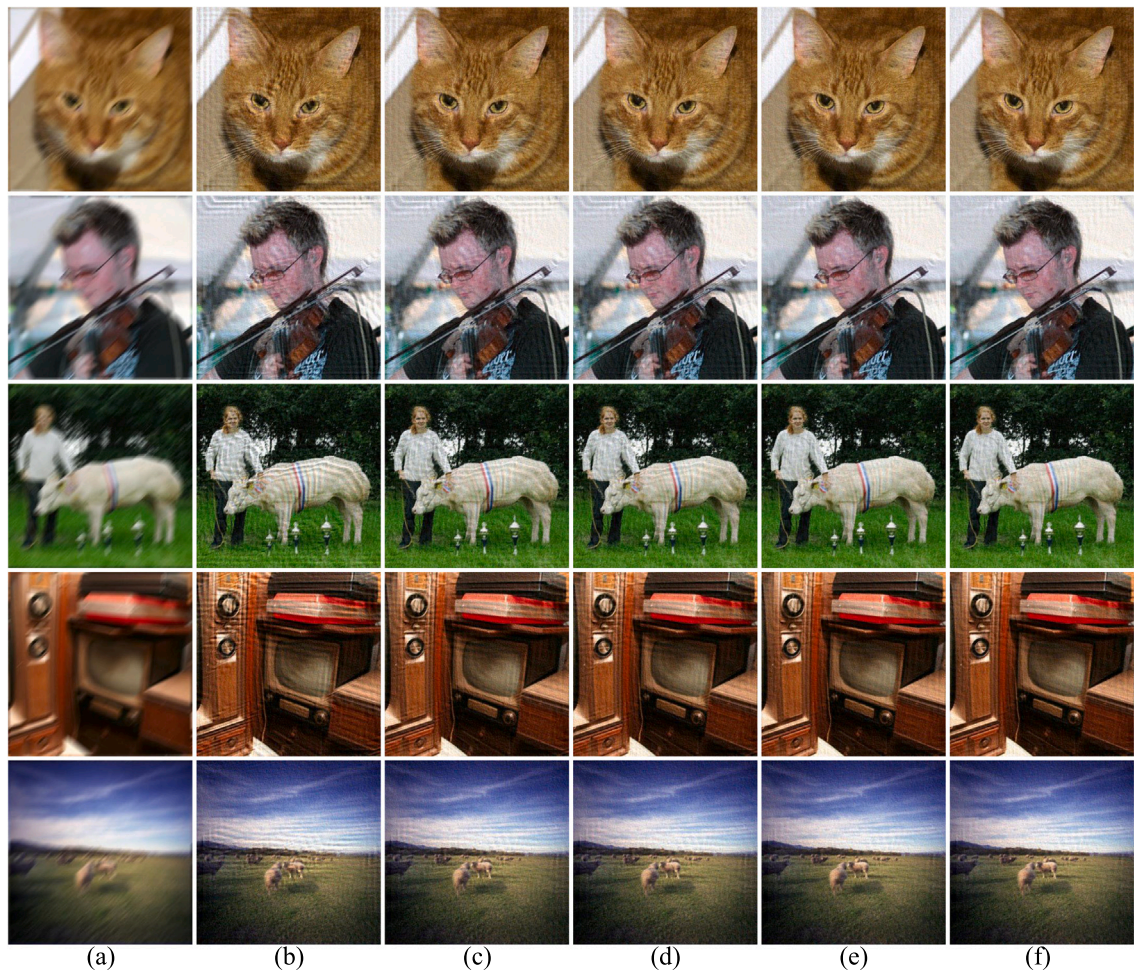
Fig. 7. Samples of deblurring results with different methods on noise VOC2012 dataset. (a) degraded image, (b) Traditional Radon-transform-based method's results, (c) RBFNN's results, (d) Wang's results, (e) Zhou's results, (f) our results.

frequency response of blurred image. Firstly, the Gaussian low-pass and high-pass filters are adopted upon the blurred image and the frequency response respectively, so as to reduce the negative impact from noise. Then we construct a self-adaptive Radon approach with batch normalization to estimate the blur parameters. We performed a series of experiments on both the synthetic VOC2012 dataset and the natural-real motion blurred image to compare our method against the existing methods by qualitative and quantitative evaluations. The experimental results show that our proposed blur kernel estimation method can obtain up to 99.21% SSIM on the deblurring task of noise-free blurred images, and 91.76% SSIM on the noisy blurred images. Overall, our method performs well with respect to a variety of blur parameters and can obtain the satisfying deblurring quality.

Although the proposed method can achieve high enough accuracy for blur angle estimation, the fact that we would like to solve in future will be the estimation of blur length. Moreover, it is worth exploring an effective solution to the problem of nonlinear and non-uniform motion blur.

Declaration of competing interest

The authors declare that they have no known competing financial interests or personal relationships that could have appeared to influence the work reported in this paper.

Acknowledgments

References

[1] W. Zhou, X. Hao, K. Wang, Z. Zhang, Y. Yu, H. Su, K. Li, X. Cao, A. Kuijper, Improved estimation of motion blur parameters for restoration from a single image, PLoS One 15 (9) (2020) e0238259.
[2] L. Yang, H. Ji, A variational em framework with adaptive edge selection for blind motion deblurring, in: Proceedings of the IEEE Conference on Computer Vision and Pattern Recognition, 2019, pp. 10167–10176.
[3] H. Sim, M. Kim, A deep motion deblurring network based on per-pixel adaptive kernels with residual down-up and up-down modules, in: Proceedings of the IEEE Conference on Computer Vision and Pattern Recognition Workshops, 2019.
[4] T. Oktay, H. Celik, I. Turkmen, Maximizing autonomous performance of fixed-wing unmanned aerial vehicle to reduce motion blur in taken images, Proc. Inst. Mech. Eng. I: J. Syst. Control Eng. 232 (7) (2018) 857–868.
[5] T. Brooks, J.T. Barron, Learning to synthesize motion blur, in: Proceedings of the IEEE Conference on Computer Vision and Pattern Recognition, 2019, pp. 6840–6848.
[6] I. Aizenberg, D.V. Paliy, J.M. Zurada, J.T. Astola, Blur identification by multilayer neural network based on multivalued neurons, IEEE Trans. Neural Netw. 19 (5) (2008) 883–898.
[7] R. Dash, B. Majhi, Motion blur parameters estimation for image restoration, Optik 125 (5) (2014) 1634–1640.
[8] D. Gong, J. Yang, L. Liu, Y. Zhang, I. Reid, C. Shen, A. Van Den Hengel, Q. Shi, From motion blur to motion flow: a deep learning solution for removing heterogeneous motion blur, in: Proceedings of the IEEE Conference on Computer Vision and Pattern Recognition, 2017, pp. 2319–2328.
[9] J. Sun, W. Cao, Z. Xu, J. Ponce, Learning a convolutional neural network for non-uniform motion blur removal, in: Proceedings of the IEEE Conference on Computer Vision and Pattern Recognition, 2015, pp. 769–777.
[10] Z. Ma, R. Liao, X. Tao, L. Xu, J. Jia, E. Wu, Handling motion blur in multi-frame super-resolution, in: Proceedings of the IEEE Conference on Computer Vision and Pattern Recognition, 2015, pp. 5224–5232.
[11] B. Ma, L. Huang, J. Shen, L. Shao, M.-H. Yang, F. Porikli, Visual tracking under motion blur, IEEE Trans. Image Process. 25 (12) (2016) 5867–5876.
[12] J. Gast, A. Sellent, S. Roth, Parametric object motion from blur, in: Proceedings of the IEEE Conference on Computer Vision and Pattern Recognition, 2016, pp. 1846–1854.
[13] Z. Xu, H. Chen, Z. Li, Blind image deblurring using group sparse representation, Digit. Signal Process. (2020) 102736.
[14] Z. Jiang, Y. Zhang, D. Zou, J. Ren, J. Lv, Y. Liu, Learning event-based motion deblurring, in: Proceedings of the IEEE/CVF Conference on Computer Vision and Pattern Recognition, 2020, pp. 3320–3329.
[15] F. Queiroz, T.I. Ren, Endoscopy image restoration: A study of the kernel estimation from specular highlights, Digit. Signal Process. 88 (2019) 53–65.
[16] J.G. Serra, J. Mateos, R. Molina, A.K. Katsaggelos, Variational EM method for blur estimation using the spike-and-slab image prior, Digit. Signal Process. 88 (2019) 116–129.
[17] S. Jiao, M. Sun, Y. Gao, T. Lei, Z. Xie, X. Yuan, Motion estimation and quality enhancement for a single image in dynamic single-pixel imaging, Opt. Express 27 (9) (2019) 12841–12854.
[18] Z. Wang, Z. Yao, Q. Wang, Improved scheme of estimating motion blur parameters for image restoration, Digit. Signal Process. 65 (2017) 11–18.
[19] V. Rengarajan, S. Zhao, R. Zhen, J. Glotzbach, H. Sheikh, A.C. Sankaranarayanan, Photosequencing of motion blur using short and long exposures, in: Proceedings of the IEEE/CVF Conference on Computer Vision and Pattern Recognition Workshops, 2020, pp. 510–511.
[20] A.M. Deshpande, S. Patnaik, A novel modified cepstral based technique for blind estimation of motion blur, Optik 125 (2) (2014) 606–615.
[21] M. Dobeš, L. Machala, T. Fürst, Blurred image restoration: A fast method of finding the motion length and angle, Digit. Signal Process. 20 (6) (2010) 1677–1686.
[22] M.A. Figueiredo, R.D. Nowak, An em algorithm for wavelet-based image restoration, IEEE Trans. Image Process. 12 (8) (2003) 906–916.
[23] T.S. Cho, S. Paris, B.K. Horn, W.T. Freeman, Blur kernel estimation using the radon transform, in: CVPR 2011, IEEE, 2011, pp. 241–248.
[24] H. Hong, I.K. Park, Single-image motion deblurring using adaptive anisotropic regularization, Opt. Eng. 49 (9) (2010) 097008.
[25] S. Cho, S. Lee, Fast motion deblurring, ACM Trans. Graph. 28 (5) (2009) 145.
[26] Q. Shan, J. Jia, A. Agarwala, High-quality motion deblurring from a single image, Acm Trans. Graph. (Tog) 27 (3) (2008) 73.
[27] J.P. Oliveira, M.A. Figueiredo, J.M. Bioucas-Dias, Parametric blur estimation for blind restoration of natural images: Linear motion and out-of-focus, IEEE Trans. Image Process. 23 (1) (2013) 466–477.
[28] A.M. Deshpande, S. Patnaik, A novel modified cepstral based technique for blind estimation of motion blur, Optik 125 (2) (2014) 606–615.
[29] M.E. Moghaddam, M. Jamzad, Motion blur identification in noisy images using mathematical models and statistical measures, Pattern Recognit. 40 (7) (2007) 1946–1957.
[30] R. Lokhande, K. Arya, P. Gupta, Identification of parameters and restoration of motion blurred images, in: Proceedings of the 2006 ACM Symposium on Applied Computing, 2006, pp. 301–305.
[31] M. Sakano, N. Suetake, E. Uchino, A psf estimation based on hough transform concerning gradient vector for noisy and motion blurred images, IEICE Trans. Inf. Syst. 90 (1) (2007) 182–190.
[32] M. Tanaka, K. Yoneji, M. Okutomi, Motion blur parameter identification from a linearly blurred image, in: 2007 Digest of Technical Papers International Conference on Consumer Electronics, IEEE, 2007, pp. 1–2.
[33] M. Everingham, L. Van Gool, C.K.I. Williams, J. Winn, A. Zisserman, Visual object classes challenge 2012 dataset (voc2012), 2012, http://host.robots.ox.ac.uk/pascal/VOC/voc2012/.